Computers and Mathematics with Applications 201 (2026) 248–258

Contents lists available at ScienceDirect

Computers and Mathematics with Applications

journal homepage: www.elsevier.com/locate/camwa

Pinning phenomena in numerical schemes of the Allen–Cahn equation

Junseok Kim [a], Zhengang Li [b], Xinpei Wu [a], Soobin Kwak [a,*]

[a] Department of Mathematics, Korea University, Seoul, 02841, Republic of Korea
[b] Program in Actuarial Science and Financial Engineering, Korea University, Seoul, 02841, Republic of Korea

ARTICLE INFO

MSC:
65M06
65M12

Keywords:
Pinning phenomena
Allen–Cahn equation
Numerical scheme

ABSTRACT

In this study, we investigate the artificial pinning phenomena that emerge in numerical simulations of high-order Allen–Cahn (AC) equations. The AC equation is widely used to describe interface motion during phase separation processes. However, discretized numerical solutions may exhibit nonphysical behavior such as interface immobilization, or "pinning," particularly when the ratio between the interfacial thickness model parameter (ϵ) and the spatial numerical mesh size (h) is below a critical threshold. The present work systematically analyzes how this ratio, $P = \epsilon/h$, influences interface dynamics and determines the critical values at which pinning begins to occur for various nonlinearity degrees (α) of the polynomial potential. A fully explicit finite difference method is used to simulate the AC equation in both two- and three-dimensional settings. A bisection algorithm is introduced to accurately identify the critical pinning threshold P^* as a function of α. Numerical experiments demonstrate that as α increases, P^* decreases, indicating that the solution becomes more sensitive to spatial discretization and requires finer grids to avoid artificial pinning. Additionally, computational results show that higher values of α yield thicker and smoother interface transitions, and the study also investigates the influence of these values on phase morphology under random initial conditions. The numerical results in this study provide quantitative guidance for selecting discretization parameters in phase-field simulations and emphasize the importance of balancing the interface resolution with model complexity. These insights contribute to the development of accurate and robust numerical schemes for simulating interfacial dynamics in complex physical systems.

1. Introduction

The phase-field method provides a powerful methodology for modeling interfacial dynamics in various scientific and engineering applications, such as materials science [1,2], fluid dynamics, and image processing [3]. By introducing a continuous order parameter to implicitly represent interfaces, it avoids the need for explicit interface tracking [4]. The temporal evolution of this phase-field variable is typically governed by a class of partial differential equations (PDEs), such as the Allen–Cahn (AC) or Cahn–Hilliard (CH) equations [5,6]. In particular, the AC equation is widely used to model interface motion driven by curvature without mass conservation. Despite its modeling advantages, numerical simulations of the AC equation face significant challenges [7], including accurately resolving interfaces, preserving energy dissipation properties, and avoiding nonphysical artifacts such as pinning. The pinning phenomenon

* Corresponding author.
E-mail address: soobin23@korea.ac.kr (S. Kwak).

https://doi.org/10.1016/j.camwa.2025.11.001
Received 26 June 2025; Received in revised form 26 September 2025; Accepted 4 November 2025

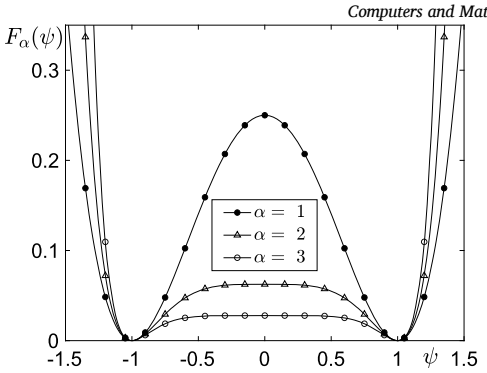

Fig. 1. $F_\alpha(\psi(\mathbf{x},t)) = \left((\psi(\mathbf{x},t))^{2\alpha} - 1\right)^2/(4\alpha^2)$ for the cases $\alpha = 1, 2$, and 3.

[8] refers to cases in numerical simulations or physical processes where an interface becomes "stuck" and unable to move freely. In numerical simulations, when ϵ/h is small, which means that the interface is narrow relative to the mesh size, pinning phenomena often occur due to insufficient spatial resolution [9]. Alber [10] studied the dependence of interface velocity on interface energy and width in the AC model and pointed out that if the mesh resolution is insufficient, the interface may not propagate smoothly; therefore, the use of adaptive mesh and other advanced numerical methods is required. Nepomnyashchy [11] studied coarsening, which is a gradual growth of the characteristic scale with time, and pattern formation in physical systems using the AC and CH equations. The work also discussed factors that can slow down or arrest coarsening, such as wall pinning, oscillatory tails, and nonlocal interactions.

This study applies the bisection method to approximate the threshold value of ϵ/h at which the pinning phenomenon occurs. The numerical scheme is an explicit finite difference method (FDM) of the AC equation with a high-order polynomial potential, given as follows:

$$\frac{\partial \psi(\mathbf{x},t)}{\partial t} = -\frac{F'_\alpha(\psi(\mathbf{x},t))}{\epsilon^2} + \Delta\psi(\mathbf{x},t), \quad \mathbf{x} \in \Omega, \ t > 0. \tag{1}$$

Here, $\psi(\mathbf{x},t)$ evolves over the spatial domain $\Omega \in \mathbb{R}^d$, where $d = 2$ and 3. The function $F_\alpha(\psi)$ represents the double-well potential, and ϵ denotes the interface thickness parameter. In this paper, the zero Neumann boundary condition is applied as $\mathbf{n} \cdot \nabla\psi(\mathbf{x},t) = 0$ on $\partial\Omega$. Here, $\mathbf{n}$ is normal to $\partial\Omega$. The high-order polynomial free energy potential is as follows:

$$F_\alpha(\psi(\mathbf{x},t)) = \frac{1}{4\alpha^2}\left((\psi(\mathbf{x},t))^{2\alpha} - 1\right)^2, \tag{2}$$

where α is a positive integer. Fig. 1 illustrates the high-order polynomial free energy profiles for different values of α. We observe that when $\alpha = 1$, Eq. (2) reduces to the canonical AC equation [12], which governs the temporal evolution of a scalar order parameter during phase separation. The AC equation is used in numerous fields, such as fluid dynamics [13], image processing [14,15], topology optimization [16,17], geometric flows [18,19], tumor growth [20], and data segmentation [21]. For $\alpha > 1$, which represents the high-order case, we observe that during temporal evolution the noise is effectively damped, as shown in Fig. 2. This property suggests potential applicability in practical tasks such as data classification.

Considering the inherent nonlinearity and stiffness of the AC equation, the exact analytical solutions are generally unattainable. That is why numerical techniques are indispensable for obtaining approximate solutions. Hussain et al. [23] applied the variational iteration method to derive a convergent approximate analytical series solution of the AC equation and demonstrated its good agreement with hyperbolic, traveling-wave, and finite difference numerical solutions. Sohaib et al. [24] used the spectral method to solve the space fractional AC equation numerically and showed that varying fractional orders markedly affected solution stabilization rates, interface sharpness, and energy dissipation. Uzunca and Karasözen [25] developed two-step linearly implicit schemes for the AC model by polarizing the free-energy functional. These methods preserve energy dissipation and demonstrated accuracy through numerical experiments in one, two, and three dimensions. Haq et al. [26] formed a numerical method using non-polynomial spline functions combined with forward time differencing to approximate solutions of the PHI-Four and AC equations. They demonstrated unconditional stability and improved accuracy over existing methods through convergence analysis and numerical tests. Hu et al. [27] further extended energy-stable schemes to curved geometries and developed a second-order accurate method for the Lifshitz–Petrich equation on curved surfaces. Xia et al. [28] proposed an unconditionally energy-stable approach for solving the Swift–Hohenberg equation on arbitrarily curved surfaces. Numerical experiments have verified that certain computational schemes for the AC equation preserve key physical properties, such as the maximum principle and energy conservation. Additionally, conservative formulations and corresponding numerical methods have been developed to maintain mass conservation. Yang et al. [29] constructed a class of up to fourth-order temporal unconditionally structure-preserving methods for the AC equation and its conservative forms using mass-lumping finite element discretization combined with integrating-factor Runge–Kutta and stabilization techniques, and they verified high-order accuracy, maximum-principle preservation, mass conservation, and energy stability through numerical experiments. Cai et al. [30] developed a spatial finite-difference scheme that decoupled the updates into scalar nonlinear solves to yield highly efficient, linearly implicit energy-conservative or dissipative integrators for the sine-Gordon and AC equations, connected this framework to Itoh-Abe discrete-gradient and partitioned averaged-vector-field techniques, and showed its natural parallelism and low complexity

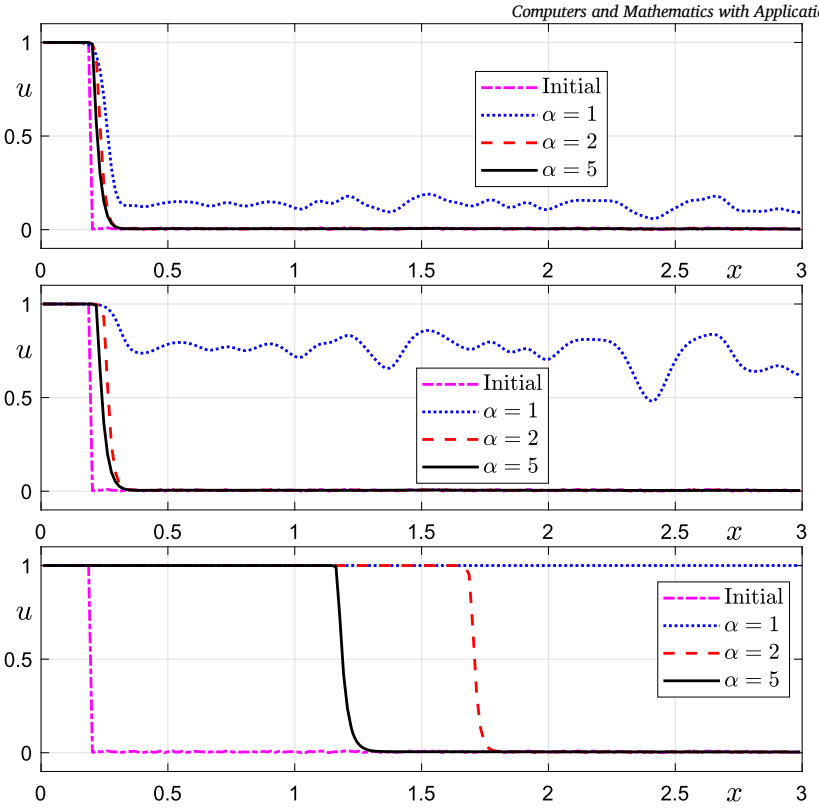

Fig. 2. Temporal evolution of a traveling wave solution with noise. Figure reprinted from [22] under the Creative Commons Attribution License (CC BY).

through numerical experiments. Li et al. [31] proposed stable schemes for surface CH systems an extended phase-field methods to complex geometries. Adopting polynomial free-energy functions of order greater than four enables precise control of interface sharpness and propagation speed, which leads to the formation of sharper phase boundaries and a reduction in numerical noise to improve application performance. Moreover, these high-order potentials permit multiple equilibrium states, which are essential for modeling complex interactions in materials science and biological systems. To approximate the resulting high-order AC equations, researchers have developed various numerical schemes, including unconditionally energy-stable algorithms [32–34], conservative formulations [35–37], and maximum-principle-preserving methods [29,38].

In the present study, we investigate the pinning of phase interfaces that can occur when numerically discretizing the high-order AC equation with polynomial free-energy potentials. We use an explicit method, noting that the high-order AC equation, compared with the classical AC equation, admits a slightly more restrictive time step limitation [39]. Although the frozen-coefficient method [40] can be applied to relieve this restriction, the present work focuses instead on the pinning effects associated with the interface thickness parameter ϵ and the high-order parameter α coupled with numerical discretization. Particular emphasis is placed on how the ratio of the spatial mesh size h to the interfacial parameter ε governs the immobilization of interfaces in practice. Our objective is to establish quantitative criteria for choosing ϵ relative to h, thereby precluding spurious pinning and ensuring faithful resolution of interface motion. These results provide actionable guidelines for designing stable and accurate computational methods in phase-field simulations.

This article is organized as follows: In Section 2, we present the numerical algorithm for the high-order AC equations. In Section 3, we present numerical tests. In Section 4, we summarize the findings.

2. Numerical solution algorithms

We introduce fully explicit FDMs for the AC equation and begin by examining the equation in a two-dimensional (2D) domain $\Omega = (L_x, R_x) \times (L_y, R_y)$ with a number of spatial grid points N_x and N_y. A uniform spatial grid size $h = (R_x - L_x)/N_x$ is applied. The discretized domain is defined as $\Omega_h = \{(x_p, y_q) \mid x_p = L_x + (p - 0.5)h,\ y_q = L_y + (q - 0.5)h,\ \ p = 1, 2, \dots, N_x,\ q = 1, 2, \dots, N_y\}$. On the computational domain, $\psi(x_p, y_q, n\Delta t)$ is approximated by ψ_{pq}^n for $n = 1, 2, \dots, N_t$. Here, T is the final time, N_t is the number of time steps, and $\Delta t = T/N_t$ is the time step. We use the explicit Euler method for temporal discretization as follows:

$$\frac{\psi_{pq}^{n+1} - \psi_{pq}^n}{\Delta t} = -\frac{(\psi_{pq}^n)^{2\alpha-1}\left((\psi_{pq}^n)^{2\alpha} - 1\right)}{\alpha\epsilon^2}$$

$$+\frac{\psi^n_{p-1,q}+\psi^n_{p+1,q}+\psi^n_{p,q-1}+\psi^n_{p,q+1}-4\psi^n_{pq}}{h^2}.$$

For the 2D computational domain, the zero Neumann boundary condition is applied as follows:

$$\psi_{0q}=\psi_{1q} \text{ and } \psi_{N_x+1,q}=\psi_{N_xq}, \text{ for } q=1,2,\dots,N_y, \tag{3}$$

$$\psi_{p0}=\psi_{p1} \text{ and } \psi_{p,N_y+1}=\psi_{pN_y}, \text{ for } p=1,2,\dots,N_x. \tag{4}$$

Then, we define the AC equation in the three-dimensional (3D) domain $\Omega=(L_x,\ R_x)\times(L_y,\ R_y)\times(L_z,\ R_z)$ with number of spatial grid points $N_x,\ N_y$ and N_z. A uniform spatial grid size $h=(R_x-L_x)/N_x$ is applied. Let us consider the discretized domain $\Omega_h=\{(x_p,y_q,z_r)\mid x_p=L_x+(i-0.5)h,\ y_q=L_y+(j-0.5)h,\ z_r=L_z+(k-0.5)h\ \ p=1,2,\dots,N_x,\ q=1,2,\dots,N_y,\ r=1,2,\dots,N_z\}$. On the discretized domain, $\psi(x_p,y_q,z_r,n\Delta t)$ is approximated as ψ^n_{pqr} for $n=1,2,\dots,N_t$. We use the explicit Euler method for temporal discretization. Therefore, we have the following equation using the 7-point stencil discrete Laplacian operator.

$$\frac{\psi^{n+1}_{pqr}-\psi^n_{pqr}}{\Delta t}=-\frac{(\psi^n_{pqr})^{2\alpha-1}\left((\psi^n_{pqr})^{2\alpha}-1\right)}{\alpha\epsilon^2}$$
$$+\frac{\psi^n_{p+1,qr}+\psi^n_{p-1,qr}+\psi^n_{p,q+1,r}+\psi^n_{p,q-1,r}+\psi^n_{pq,r+1}+\psi^n_{pq,r-1}-6\psi^n_{pqr}}{h^2}.$$

For the 3D numerical domain, the zero Neumann boundary condition is applied as follows:

$$\psi_{0qr}=\psi_{1qr} \text{ and } \psi_{N_x+1,qr}=\psi_{N_x,qr}, \text{ for } q=1,2,\dots,N_y,\ r=1,2,\dots,N_z, \tag{5}$$

$$\psi_{p0r}=\psi_{p1r} \text{ and } \psi_{p,N_y+1,r}=\psi_{pN_yr}, \text{ for } p=1,2,\dots,N_x,\ r=1,2,\dots,N_z, \tag{6}$$

$$\psi_{pq0}=\psi_{pq1} \text{ and } \psi_{pq,N_z+1}=\psi_{pqN_z}, \text{ for } p=1,2,\dots,N_x,\ q=1,2,\dots,N_y. \tag{7}$$

We apply explicit difference schemes. Therefore, the following stability condition must be satisfied to ensure reliability of the numerical solution:

$$\Delta t\le\frac{\epsilon^2h^2}{2(h^2+d\epsilon^2)}, \quad \text{for } d=2,3, \tag{8}$$

where d denotes the spatial dimension. The corresponding proofs for the 2D and 3D cases can be found in [39] and [41], respectively.

In our proposed method, we use the bisection method to find the critical point P^* such that the pinning phenomenon would start to occur. The P value is defined as $P=\epsilon/h$. Below, we illustrate this algorithm in pseudo-code Algorithm 1. We note that all numerical experiments in this study are conducted using MATLAB R2024b in double precision arithmetic (float64). In the case where computations are performed in single precision arithmetic (float32), the criterion for detecting the pinning phenomenon should be adjusted, and the tolerance 10^{-6} can be used instead of 10^{-10}.

Algorithm 1: Bisection algorithm to approximate P^*.

Input: L_P: Lower bound; U_P: Upper bound; $\psi_0(\mathbf{x})$: Initial state; tol: Tolerance
Output: An approximation P^* satisfying the given tolerance
while $U_P-L_P>tol$ **do**
  $P=\dfrac{L_P+U_P}{2}$;
  Solve the AC equation with $\epsilon=Ph$ to observe the behavior of ψ;
  if $\max\psi^{n+1}<0$ **then** ▷ Determine whether ψ would undergo finite-time extinction
    $U_P=P$;
    break
  end
  else if $\|\psi^{n+1}-\psi^n\|_\infty<10^{-10}$ **then** ▷ Determine whether ψ would undergo pinning phenomenon
    $L_P=P$;
    break
  end
end
return $P^*=L_P$

We note that, in this study, the bisection method is used because of its robustness and simplicity. Although the critical value P^* can, in principle, be approximated by higher-order methods such as the secant method, we adopt the bisection approach to guarantee reliability and ease of implementation.

3. Numerical tests

This section presents a series of computational experiments designed to determine the critical value of the parameter ratio $P=\epsilon/h$ at which numerical interface pinning arises in the discretized AC equations governed by the high-order polynomial energy functionals. The numerical tests are conducted in both 2D and 3D domains to validate the robustness of the proposed criteria. Unless otherwise

Table 1
The critical values of P.

α	1	2	3	4	5	6
P^*	0.550000	0.334375	0.296875	0.287500	0.278125	0.259375

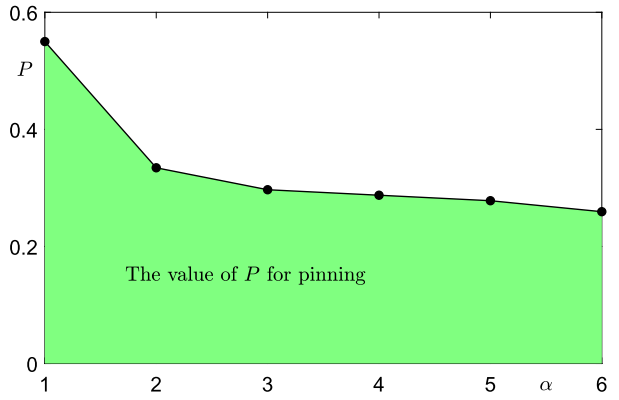

Fig. 3. The region of P values in which the pinning phase occurs.

stated, the 2D numerical tests are performed with the homogeneous Neumann boundary conditions given in Eqs. (3) and (4), and the 3D numerical tests are conducted with the zero Neumann boundary conditions specified in Eqs. (5)–(7).

3.1. Two-dimensional test

We conduct a set of numerical tests to obtain the critical point of P for different values of α. To impose a sharp interface at the initial stage, we prescribe a stiff initial condition of the order parameter $\psi(x, y, 0)$ as follows:

$$\psi(x, y, 0) = \begin{cases} 1 & \text{if } \sqrt{x^2 + y^2} < 0.5 \\ -1 & \text{otherwise,} \end{cases}$$

which corresponds to a circular inclusion of radius 0.5 centered at the origin, embedded in a background phase of value -1. The computational domain is chosen as $\Omega = (-0.7, 0.7) \times (-0.7, 0.7)$, which provides sufficient space for the evolution of the phase interface without the influence of boundary effects. The simulation parameters are set as $N_x = N_y = 140$ and $\Delta t = 0.9\Delta t_{\max}$, where $\Delta t_{\max} = 0.5(\epsilon h)^2/(h^2 + 2\epsilon^2)$ denotes the maximum stable time step which guarantees numerical stability under the adopted discretization scheme [39].

Table 1 summarizes the critical values of the parameter P^* for different values of α. These values correspond to the threshold ratio ϵ/h at which the phase interface of ψ becomes pinned and ceases to propagate. The pinning phenomenon indicates the balance between interfacial energy and discretization resolution. As shown in Table 1, P^* decreases monotonically as α increases, which indicates that the critical resolution requirement becomes less stringent for larger α. This trend reflects the strong dependence of the interface pinning threshold on α, and demonstrates that the discretization must be sufficiently fine to capture accurate dynamics when α is small.

Fig. 3 illustrates the region of P values for which pinning occurs. The shaded region indicates the values of ϵ that result in the phase of ψ remaining pinned under all tested conditions.

Figs. 4(a) and 4(c) show the pinned interface of ψ at the corresponding critical values listed in Table 1. Figs. 4(b) and 4(d) provide a further indication of the shape of the solutions under the pinning state. By extracting the level contours at -0.9 and 0.9, we are able to compare the morphology of the solution under different values of α. Figs. 4(c) and 4(f) show the number of spatial grid points located between the -0.9 and 0.9 level contours of ψ. This observation suggests that the thickness of the interface governed by the pinning condition increases for larger values of α.

Fig. 5 shows the values of the discrete Laplacian $\Delta_h\psi$. As the value of α increases, the interface thickness becomes thicker, which in turn results in smaller values of the discrete Laplacian of the pinned ψ. This implies that the interface becomes smoother for larger values of α.

We observe the phase separation phenomenon for various high-order values of α. The initial condition in $\Omega = (-1, 1) \times (-1, 1)$ is given by

$$\psi(x, y, 0) = 0.5 \sin(3\pi x) \sin(3\pi y) + 0.5\text{rand}(x, y),$$

where $\text{rand}(x, y)$ denotes a random value drawn from a normal distribution within the interval $(-1, 1)$. The grid step size h is set to 0.01, and time step size Δt is set to $0.9\Delta t_{\max}$. For each value of α, we use $\epsilon = 0.8P^*h$.

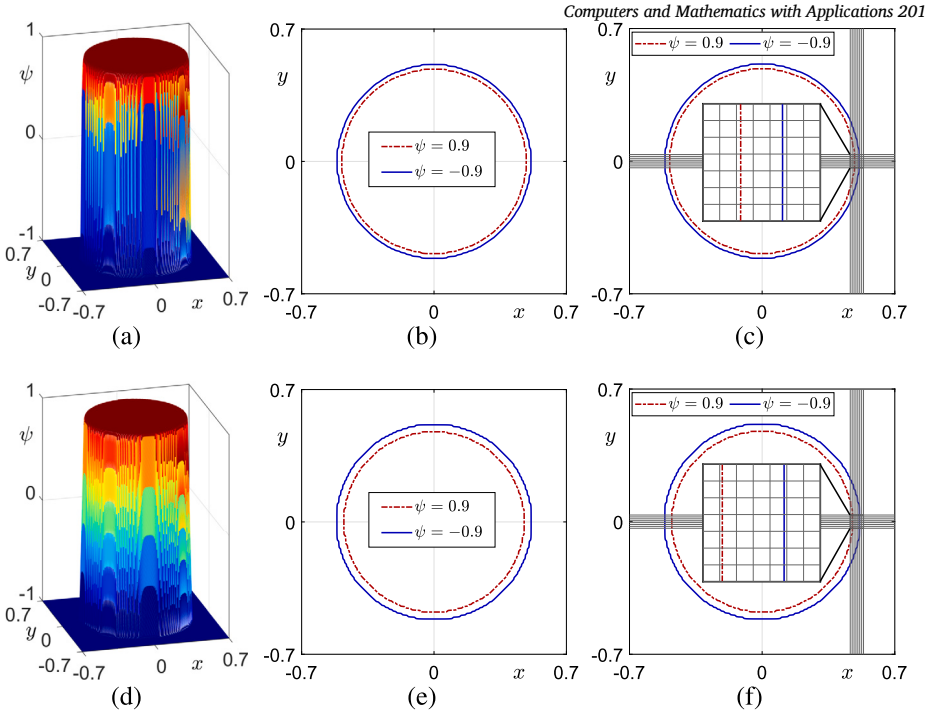

Fig. 4. (a) and (d): Solutions of ψ with the critical value of P. (b) and (e): The -0.9 and 0.9 level contours of ψ at the critical value P^*. (c) and (f): Detailed views of the contour in (b) and (e), respectively. The top and bottom rows correspond to $\alpha = 1$ and 6, respectively.

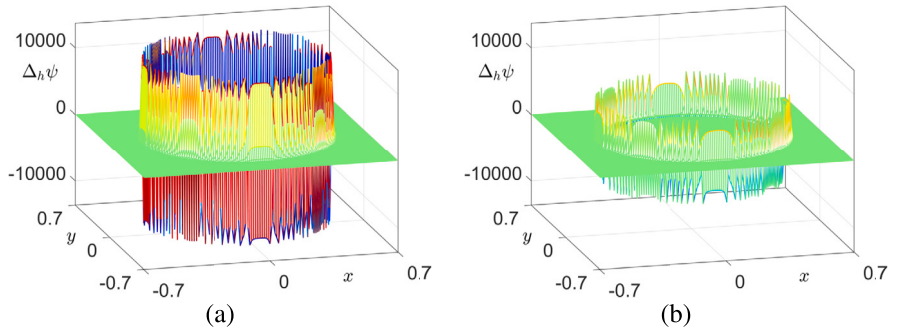

Fig. 5. The solution of Laplace operator $\Delta_h\psi$ with the critical value of P^*. (a) and (b) correspond to $\alpha = 1$ and 6, respectively.

Fig. 6 illustrates the phase separation phenomenon for various values of the nonlinearity parameter α. The initial condition consists of a trigonometric function combined with spatial randomness, which serves to promote symmetry breaking. As α increases, the resulting phase structures present a significant difference in interfacial smoothness and geometric complexity. For $\alpha = 1$, the interface between the two phases is highly irregular, with many small-scale features and curved boundaries. This reflects the dominance of the diffusive term relative to the nonlinear term in driving the evolution. At $\alpha = 3$, the interfaces begin to form more regular and orthogonal patterns. This behavior reflects the increased influence of the nonlinear potential that favors sharper separation between the two phases. When $\alpha = 6$, the interface geometry becomes markedly simplified and smoother, with fewer, larger domains and minimal curvature. This result indicates that strong nonlinearity suppresses fine-scale features and promotes stabilization of coarser structures. Overall, the results demonstrate that the parameter α, which controls the intensity of the nonlinear term, affects the morphology of the phase separated pattern.

We observe the pinning effect for arbitrarily complex initial conditions as α varies. The numerical domain is set as $\Omega = (-1, 1)\times(-1, 1)$ with a mesh resolution of 50×50. Numerical computational tests are conducted for three different values of $\alpha = 1, 3, 6$. All other parameters are used equally in the previous test. Fig. 7 illustrates the pinned phases observed during temporal evolution starting from an arbitrary initial condition for three representative values of the parameter α. The first row displays the corresponding two-dimensional contour plots, which show distinct phase interfaces and clearly indicate interface pinning through stationary boundaries. In the second row, the number of spatial grid points between the interfaces where $-0.9 < \psi < 0.9$ can be observed. The third row presents three-dimensional mesh plots, where the interface transition becomes thicker and interface complexity decreases as α increases from 1 to 6.

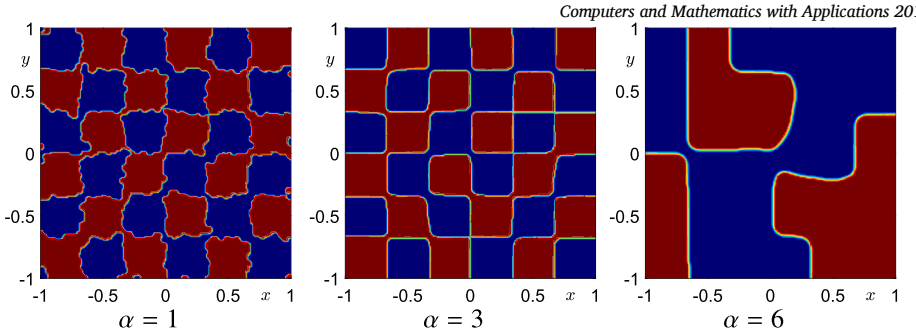

Fig. 6. Phase separation phenomenon with various values of α.

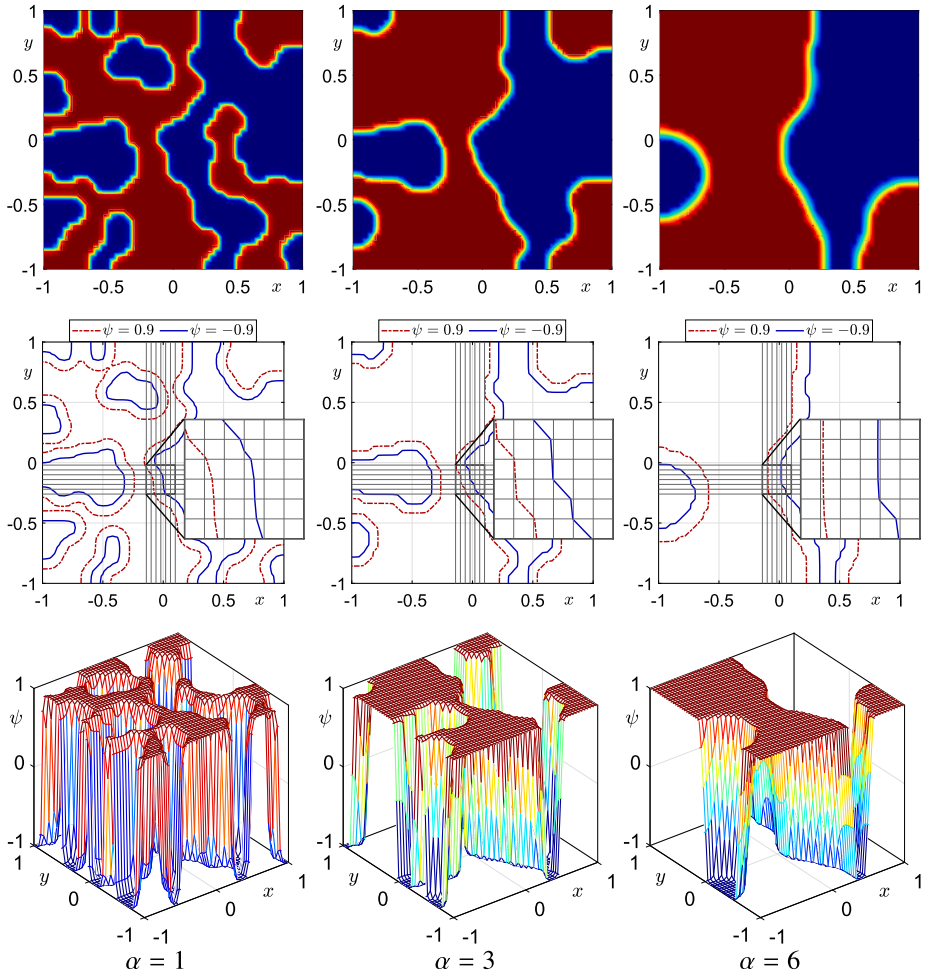

Fig. 7. Pinned phase evolution from an arbitrary initial condition for $\alpha = 1, 3$, and 6. Larger α values yield thicker interfaces and smoother pinned structures, as seen in contour and surface plots.

3.2. Three-dimensional test

We perform numerical experiments to determine the critical point of P at which pinning occurs. The system is initialized with a sharp phase boundary given by

$$\psi(x, y, 0) = \begin{cases} 1 & \text{if } \sqrt{x^2 + y^2 + z^2} < 0.5 \\ -1 & \text{otherwise} \end{cases},$$

Table 2
The critical value of P.

α	1	2	3	4	5	6
P^*	0.409375	0.240625	0.212500	0.193750	0.184375	0.175000

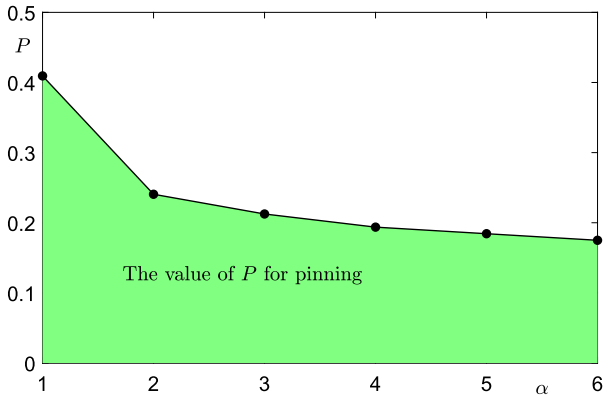

Fig. 8. The region of P values in which the pinning phase occurs.

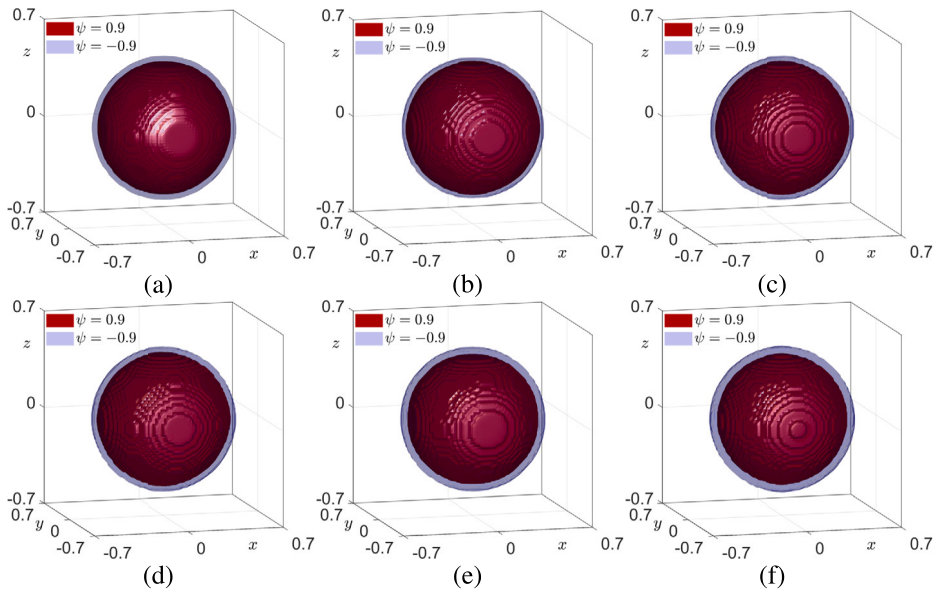

Fig. 9. Snapshots of the −0.9 and 0.9 level isosurfaces of the solution ψ at the critical value of P. (a)–(f) correspond to $\alpha = 1, \ldots, 6$, respectively.

within $\Omega = (-0.7, 0.7) \times (-0.7, 0.7) \times (-0.7, 0.7)$. The mesh resolution is specified as $N_x = N_y = N_z = 70$, with a time step of $\Delta t = 0.9\Delta t_{\max}$, where $\Delta t_{\max} = 0.5(\epsilon h)^2/(h^2 + 3\epsilon^2)$. The critical values of P, corresponding to the onset of pinning for different values of α, are summarized in Table 2.

Fig. 8 presents the range of P values within which pinning is observed. The shaded region denotes the corresponding values of ϵ that consistently result in the phase field ψ remaining pinned under all examined conditions.

Fig. 9 illustrates the isosurface configurations of the solution ψ at the critical values of P identified in Table 2, where pinning occurs. Figs. 9(a)–(f) corresponds to $\alpha = 1, \ldots, 6$. The visualization presents two surfaces: the inner surface represents the $\psi = 0.9$ level, while the outer surface corresponds to the $\psi = -0.9$ level. The nearly concentric and stable spherical layers demonstrate that the pinned phase remains well confined within the domain across all tested values of α, with the interface thickness gradually increasing as α becomes larger.

We consider an arbitrary random initial condition for three different values of $\alpha = 1,\ 3,\ 6$. The simulation is conducted on $\Omega = (0, 1) \times (0, 1) \times (0, 1)$, using $h = 0.02$ and $\Delta t = 0.9\Delta t_{\max}$. The parameter ϵ is chosen based on the critical pinning value P^*, such that $\epsilon = 0.8P^*h$. Fig. 10 presents the steady state configurations of ψ for $\alpha = 1$, 3, and 6. As α increases, the interface evolves from a highly fragmented, noise-preserving pattern ($\alpha = 1$) to a more organized, coarser structure with reduced geometric complexity ($\alpha = 6$).

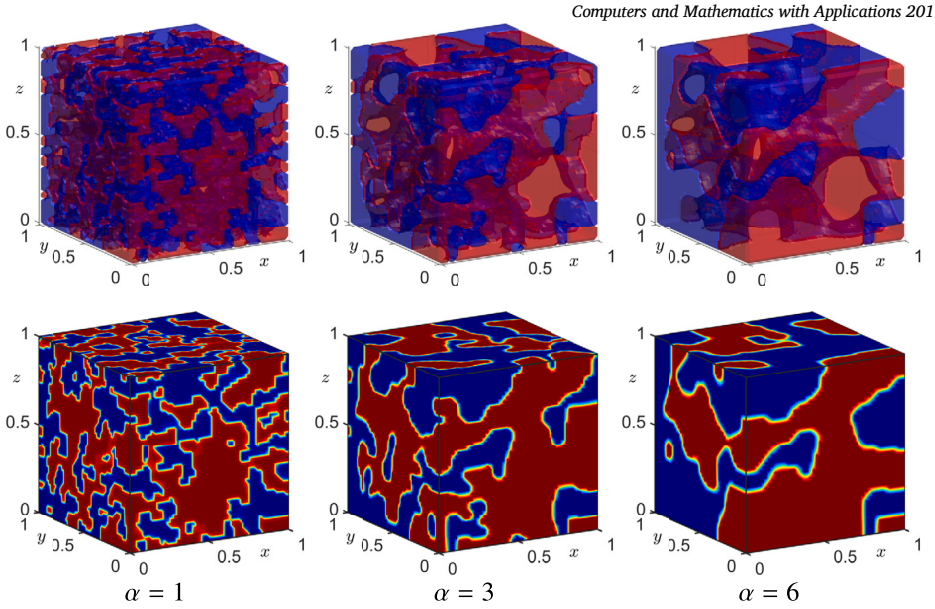

Fig. 10. The pinned interface profiles for three different values of α, with an arbitrary initial condition. Top row: isosurfaces of the computed phase fields. Bottom row: corresponding contour representations extracted from the top row configurations.

This behavior indicates that higher nonlinearity causes thicker, smoother transitions and promotes interface pinning by reducing the motion of fine-scale structures.

Finally, to briefly summarize the results of both 2D and 3D simulations, we observe that increasing α results in smoother and coarser interfaces. This behavior is particularly evident when the initial condition contains spatial randomness. In such cases, low values of α result in noise-sensitive structures, whereas high values of α produce smooth interfaces. Our results also indicate that the critical value P^* at which interface pinning occurs decreases as α increases, signifying that higher-order potentials are more sensitive to discretization effects and thus require finer spatial resolution to prevent artificial pinning. Furthermore, the thickness of the pinned interface, characterized by the number of grid points between $\psi = -0.9$ and $\psi = 0.9$, is observed to grow with increasing α, which confirms that stronger nonlinearity promotes the formation of thicker transition layers.

4. Conclusions

This study examined the occurrence of artificial pinning phenomena in numerical solutions of the high-order AC equations. The study focused on the relationship between the interfacial parameter ϵ and the spatial discretization size h, showing how their ratio significantly influences interface immobilization. Numerical experiments conducted in both two-dimensional and three-dimensional settings demonstrated that the critical threshold $P^* = \epsilon/h$ decreases as the order α of the potential increases. This indicates that higher-order nonlinearities increase sensitivity to discretization and demand finer spatial resolution to prevent artificial pinning. The results also showed that the interface thickness at the critical pinning threshold increases with larger values of α, which produces smoother and broader phase boundaries. When initial conditions include spatial randomness, lower values of α result in more complex and noise-sensitive patterns, whereas higher values yield simpler and more stable morphologies. These findings provide practical guidance for choosing model parameters in numerical simulations and contribute to the development of robust computational schemes that can accurately capture interfacial dynamics without introducing spurious numerical artifacts.

CRediT authorship contribution statement

Junseok Kim: Conceptualization, Formal analysis, Methodology, Project administration, Supervision, Validation, Writing – original draft, Writing – review & editing. **Zhengang Li**: Data curation, Investigation, Methodology, Software, Visualization, Writing – original draft, Writing – review & editing. **Xinpei Wu**: Data curation, Investigation, Methodology, Software, Visualization, Writing – original draft, Writing – review & editing. **Soobin Kwak**: Conceptualization, Data curation, Formal analysis, Investigation, Methodology, Software, Validation, Visualization, Writing – original draft, Writing – review & editing.

Acknowledgements

The first author (J.S. Kim) was supported by Korea University Grant K2504591. The corresponding author (S. Kwak) was supported by the Brain Korea 21 FOUR. We are grateful to the reviewers for their insightful feedback, which helped improve the quality of this work.

Data availability

No data was used for the research described in the article.

References

[1] W. Xie, Z. Wang, J. Kim, X. Sun, Y. Li, A novel ensemble Kalman filter based data assimilation method with an adaptive strategy for dendritic crystal growth, J. Comput. Phys. 524 (2025) 113711, https://doi.org/10.1016/j.jcp.2024.113711.
[2] Y. Li, K. Qin, Q. Xia, J. Kim, A second-order unconditionally stable method for the anisotropic dendritic crystal growth model with an orientation-field, Appl. Numer. Math. 184 (2023) 512–526, https://doi.org/10.1016/j.apnum.2022.11.006.
[3] X. Song, Q. Xia, J. Kim, Y. Li, An unconditional energy stable data assimilation scheme for Navier–Stokes–Cahn–Hilliard equations with local discretized observed data, Comput. Math. Appl. 164 (2024) 21–33, https://doi.org/10.1016/j.camwa.2024.03.018.
[4] W. Xie, Q. Xia, Q. Yu, Y. Li, An effective phase field method for topology optimization without the curvature effects, Comput. Math. Appl. 146 (2023) 200–212, https://doi.org/10.1016/j.camwa.2023.06.037.
[5] X. Song, B. Xia, Y. Li, An efficient data assimilation based unconditionally stable scheme for Cahn–Hilliard equation, Comput. Appl. Math. 43 (3) (2024) 121, https://doi.org/10.1007/s40314-024-02632-7.
[6] Z. Lv, X. Song, J. Feng, Q. Xia, B. Xia, Y. Li, Reduced-order prediction model for the Cahn–Hilliard equation based on deep learning, Eng. Anal. Bound. Elem. 172 (2025) 106118, https://doi.org/10.1016/j.enganabound.2025.106118.
[7] Q. Xia, S. Lai, J. Kim, Y. Li, Phase field modeling of melting and solidification dynamics in metallic powders during the bed fusion process, Commun. Nonlinear Sci. Numer. Simul. 108762 (2025), https://doi.org/10.1016/j.cnsns.2025.108762.
[8] W.M. Feldman, P. Morfe, The occurrence of surface tension gradient discontinuities and zero mobility for Allen–Cahn and curvature flows in periodic media, Interfaces Free Bound. 25 (4) (2023) 567–631, https://doi.org/10.4171/IFB/491.
[9] J. Zhang, Q. Du, Numerical studies of discrete approximations to the Allen–Cahn equation in the sharp interface limit, SIAM J. Sci. Comput. 31 (4) (2009) 3042–3063, https://doi.org/10.1137/080738398.
[10] H.D. Alber, Asymptotics and numerical efficiency of the Allen–Cahn model for phase interfaces with low energy in solids, Contin. Mech. Thermodyn. 29 (3) (2017) 757–803, https://doi.org/10.1007/s00161-017-0558-x.
[11] A.A. Nepomnyashchy, Coarsening versus pattern formation, C. R. Phys. 16 (3) (2015) 267–279, https://doi.org/10.1016/j.crhy.2015.03.004.
[12] S.M. Allen, J.W. Cahn, A microscopic theory for antiphase boundary motion and its application to antiphase domain coarsening, Acta Metall. 27 (6) (1979) 1085–1095, https://doi.org/10.1016/0001-6160(79)90196-2.
[13] M. Grave, A.L. Coutinho, Comparing the convected level-set and the Allen–Cahn phase-field methods in AMR/C simulations of two-phase flows, Comput. Fluids 244 (2022) 105569, https://doi.org/10.1016/j.compfluid.2022.105569.
[14] J. Budd, Y. van Gennip, J. Latz, Classification and image processing with a semi-discrete scheme for fidelity forced Allen–Cahn on graphs, GAMM-Mitt. 44 (1) (2021) e202100004, https://doi.org/10.1002/gamm.202100004.
[15] C. Liu, Z. Qiao, Q. Zhang, Multi-phase image segmentation by the Allen–Cahn Chan–Vese model, Comput. Math. Appl. 141 (2023) 207–220, https://doi.org/10.1016/j.camwa.2022.12.020.
[16] J. Gao, B. Song, Z. Mao, Structural topology optimization through implicit boundary evolution based on the Allen–Cahn equation, Eng. Optim. 53 (1) (2021) 125–144, https://doi.org/10.1080/0305215X.2019.1705288.
[17] Q. Yu, Y. Li, A second-order unconditionally energy stable scheme for phase-field based multimaterial topology optimization, Comput. Methods Appl. Mech. Eng. 405 (2023) 115876, https://doi.org/10.1016/j.cma.2022.115876.
[18] H. Li, Z. Song, J. Hu, Numerical analysis of a second-order IPDGFE method for the Allen–Cahn equation and the curvature-driven geometric flow, Comput. Math. Appl. 86 (2021) 49–62, https://doi.org/10.1016/j.camwa.2021.01.014.
[19] J. Chen, P. Gaspar, Mean curvature flow and low energy solutions of the parabolic Allen–Cahn equation on the three-sphere, J. Geom. Anal. 33 (9) (2023) 283, https://doi.org/10.1007/s12220-023-01347-1.
[20] H. Alsayed, H. Fakih, A. Miranville, A. Wehbe, Optimal control of an Allen–Cahn model for tumor growth through supply of cytotoxic drugs, Integration 2 (2022) 3–13, https://doi.org/10.3934/dcdss.2022003.
[21] M. Burger, N. Loy, A. Rossi, Asymptotic and stability analysis of kinetic models for opinion formation on networks: an Allen–Cahn approach, SIAM J. Appl. Dyn. Syst. 24 (2) (2025) 1042–1069, https://doi.org/10.1137/24M1671128.
[22] J. Kim, Modified wave-front propagation and dynamics coming from higher-order double-well potentials in the Allen–Cahn equations, Mathematics 12 (23) (2024) 3796, https://doi.org/10.3390/math12233796.
[23] S. Hussain, F. Haq, A. Shah, D. Abduvalieva, A. Shokri, Comparison of approximate analytical and numerical solutions of the Allen–Cahn equation, Int. J. Differ. Equ. 2024 (1) (2024) 8835138, https://doi.org/10.1155/2024/8835138.
[24] M. Sohaib, K.M. Furati, A. Shah, Space fractional Allen–Cahn equation and its applications in phase separation: a numerical study, Commun. Nonlinear Sci. Numer. Simul. 137 (2024) 108173, https://doi.org/10.1016/j.cnsns.2024.108173.
[25] M. Uzunca, B. Karasözen, Linearly implicit methods for Allen–Cahn equation, Appl. Math. Comput. 450 (2023) 127984, https://doi.org/10.1016/j.amc.2023.127984.
[26] M.U. Haq, S. Haq, I. Ali, M.J. Ebadi, Approximate solution of PHI-four and Allen–Cahn equations using non-polynomial spline technique, Mathematics 12 (6) (2024) 798, https://doi.org/10.3390/math12060798.
[27] X. Hu, Q. Xia, B. Xia, Y. Li, A second-order accurate numerical method with unconditional energy stability for the Lifshitz–Petrich equation on curved surfaces, Appl. Math. Lett. 163 (2025) 109439, https://doi.org/10.1016/j.aml.2024.109439.
[28] B. Xia, X. Xi, R. Yu, P. Zhang, Unconditional energy-stable method for the Swift–Hohenberg equation over arbitrarily curved surfaces with second-order accuracy, Appl. Numer. Math. 198 (2024) 192–201, https://doi.org/10.1016/j.apnum.2024.01.005.
[29] J. Yang, N. Yi, H. Zhang, High-order, unconditionally maximum-principle preserving finite element method for the Allen–Cahn equation, Appl. Numer. Math. 188 (2023) 42–61, https://doi.org/10.1016/j.apnum.2023.03.002.
[30] W. Cai, J. Ren, X. Gu, Y. Wang, Parallel and energy conservative/dissipative schemes for sine-Gordon and Allen–Cahn equations, Comput. Methods Appl. Mech. Eng. 425 (2024) 116938, https://doi.org/10.1016/j.cma.2024.116938.
[31] Y. Li, R. Liu, Q. Xia, C. He, Z. Li, First- and second-order unconditionally stable direct discretization methods for multi-component Cahn–Hilliard system on surfaces, J. Comput. Appl. Math. 401 (2022) 113778, https://doi.org/10.1016/j.cam.2021.113778.
[32] F. Guo, W. Dai, Arbitrarily high-order accurate and energy-stable schemes for solving the conservative Allen–Cahn equation, Numer. Methods Partial Differ. Equ. 39 (1) (2023) 187–212, https://doi.org/10.1002/num.22867.
[33] Z. Xu, Y. Fu, Unconditional energy stability and maximum principle preserving scheme for the Allen–Cahn equation, Numer. Algorithms (2024) 1–22, https://doi.org/10.1007/s11075-024-01880-2.
[34] B. Zhang, Y. Yang, An adaptive unconditional maximum principle preserving and energy stability scheme for the space fractional Allen–Cahn equation, Comput. Math. Appl. 139 (2023) 28–37, https://doi.org/10.1016/j.camwa.2023.02.022.

[35] L. Bu, R. Li, L. Mei, Y. Wang, On high-order schemes for the space-fractional conservative Allen–Cahn equations with local and local-nonlocal operators, Commun. Nonlinear Sci. Numer. Simul. 138 (2024) 108171, https://doi.org/10.1016/j.cnsns.2024.108171.
[36] X. Xu, Y. Hu, Y. He, J. Han, J. Zhu, High-order analysis of lattice Boltzmann models for the conservative Allen–Cahn equation, Comput. Math. Appl. 146 (2023) 106–125, https://doi.org/10.1016/j.camwa.2023.06.034.
[37] S. Aihara, N. Takada, T. Takaki, Highly conservative Allen–Cahn-type multi-phase-field model and evaluation of its accuracy, Theor. Comput. Fluid Dyn. 37 (5) (2023) 639–659, https://doi.org/10.1007/s00162-023-00655-0.
[38] J. Sun, H. Zhang, X. Qian, S. Song, Up to eighth-order maximum-principle-preserving methods for the Allen–Cahn equation, Numer. Algorithms 92 (2) (2023) 1041–1062, https://doi.org/10.1007/s11075-022-01329-4.
[39] J. Choi, S. Ham, S. Kwak, Y. Hwang, J. Kim, Stability analysis of an explicit numerical scheme for the Allen–Cahn equation with high-order polynomial potentials, AIMS Math. 9 (7) (2024) 19332–19344, https://doi.org/10.3934/math.2024941.
[40] J. Kim, Maximum principle preserving the unconditionally stable method for the Allen–Cahn equation with a high-order potential, Electron. Res. Arch. 33 (1) (2025), https://doi.org/10.3934/era.2025021.
[41] S. Ham, J. Choi, Y. Nam, J. Kim, Stability analysis of a numerical method for the 3D high-order Allen–Cahn equation, AIP Adv. 15 (1) (2025), https://doi.org/10.1063/5.0248165.